JOURNAL OF AIRCRAFT
Vol. 45, No. 5, September–October 2008

Aerodynamic Design of Micro Air Vehicles for Vertical Flight

Sergey Shkarayev*
University of Arizona, Tucson, Arizona 85721
and
Jean-Marc Moschetta† and Boris Bataille‡
Institut Supérieur de l'Aéronautique et de l'Espace, 31055 Toulouse Cedex 4, France

DOI: 10.2514/1.35573

The research and development efforts outlined in this paper address the aerodynamic design of micro air vehicles with hovering and vertical takeoff and landing capabilities. The tilt-body configuration of the vertical takeoff and landing micro air vehicle is proposed based on a propulsion system consisting of two coaxial contrarotating motors and propellers. Values of thrust, torque, power, and efficiency of this propulsion system were measured in pusher and tractor arrangements of propellers and compared against single motor-propeller propulsion. With comparable efficiency, the developed propulsion system has very little propeller torque. Hot-wire measurements have been conducted to investigate the velocity profile in slipstream. The lower average velocity and significant decrease in velocity in the core of the slipstream found in the tractor arrangement are mostly due to the parasite drag caused by the motors. It causes the decrease of the thrust force observed for the tractor arrangement in comparison with the pusher arrangement. Wind-tunnel testing was conducted for a motor, a wing, and an arrangement of a wing with a motor. The drag force on the wing is produced by two mixing airflows: freestream and propeller-induced pulsating slipstream. The zero-lift drag coefficient increases by about 4 times with propeller-induced speed increased from 0 to 7.5 m/s. The results of this study were realized in the design of a vertical takeoff and landing micro air vehicle prototype that was successfully flight tested.

Nomenclature

a = distance from propeller disk to the leading edge of the wing
C_D = drag coefficient
C_{D_0} = zero-lift drag coefficient
C_{D_P} = zero-lift drag coefficient on the part of the wing submerged into a propeller slipstream
C_L = lift coefficient
c = chord
F_{total} = total force measured by a wind-tunnel balance
P = electric power input
P_{ind} = induced power
Q = torque
R = propeller radius
R_m = maximum distance of velocity measurements from the z axis
R_s = radius of stream tube at distance s
r = motor radius
Re = mean aerodynamic chord Reynolds number
S_p = area of a part of the wing covered by propeller slipstream
S_S = area of the side wall
S_0 = wing area
T = thrust force
T_s = thrust force determined from air-velocity data
V_0 = freestream velocity
W = takeoff weight of an aircraft
$w(s)$ = induced velocity based on propeller momentum theory
w_e = measured propeller-induced velocity
ρ = air density

I. Introduction

THE truly successful use of micro air vehicle (MAV) technology is somewhat difficult without the capability of aggressive vertical maneuvering and hovering autonomously. One way to fulfill these requirements is in the design of rotary-wing MAVs (micro air vehicles), and several of these helicopters have been developed in recent years. However, they are sensitive to air turbulence due to their large rotor disc. In general, when compared with fixed-wing aircraft, rotorcraft have a smaller range, endurance, and payload capacity.

Design methods and general theoretical aerodynamic principles for large VTOL (vertical takeoff and landing) aircraft are well developed and have been summarized in the literature [1,2]. As the field of VTOL evolved, much attention was paid to propulsion system considerations and development of an aerodynamic theory for the propeller and rotor. Other subjects included design studies of configurations and control issues during hover and transition. Overall, there is a sufficient amount of relevant data and knowledge to begin exploring the VTOL concept with applications to MAVs.

In the present study, a research project on fixed-wing MAVs capable of hovering and vertical take off and landing is started, based upon previous successful designs of MAVs without these capabilities. The University of Arizona has developed one of the world's smallest mission-capable autonomous MAVs, the Dragonfly (Fig. 1) [3]. Obviously, adding hovering capabilities to these aircraft requires additional motor power to get off the ground without using the wings' aerodynamics. Another technical problem is in controlling the vehicle transition from vertical to horizontal flight. To provide effective control at low speed, the MAVs will feature large control surfaces and throws, changing the baseline design in a significant way. The present project will also benefit from an independent experimental study of the Vertigo (Fig. 1) concept

---

Received 8 November 2007; revision received 29 February 2008; accepted for publication 20 May 2008.

*Associate Professor, Department of Aerospace and Mechanical Engineering, 1130 North Mountain Avenue; svs@email.arizona.edu.AIAA. Senior Member AIAA.

†Professor, Department of Aerodynamics Energetics and Propulsion, BP 54032; jean-marc.moschetta@isae.fr.

‡Ph.D. Candidate, Department of Aerodynamics Energetics and Propulsion, BP 54032; boris.bataille@isae.fr.

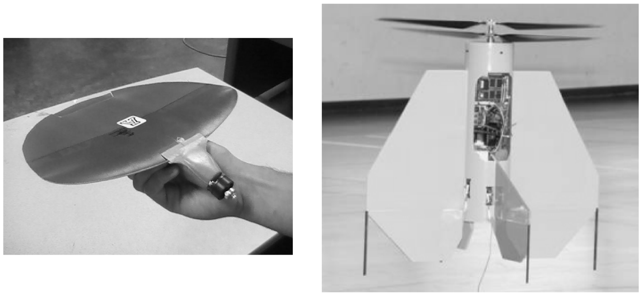

Fig. 1 Dragonfly (left) and Vertigo (right) MAV prototypes.

developed at ISAE [4]. The Vertigo consists of a fixed delta wing powered by coaxial contrarotating propellers and side-by-side motors. Its capability to hover and transition flights has been recently demonstrated on a radio-controlled prototype.

In the following discussion, two concepts for VTOL MAVs will be briefly presented, and their aerodynamics, performance, and controls will be examined. The two concepts are 1) single-propeller tilt-body aircraft and 2) contrarotating propellers tilt-body aircraft.

Aerobatic single-propeller radio-controlled (RC) aircraft emerged as a result of the integration of the latest developments in electric motor and battery technology into a lightweight structure. With a high thrust-to-weight ratio and large control surfaces and throws, these airplanes can perform spectacular aerobatic maneuvers. However, they feature very low wing loading, resulting in a very low flight speed.

In general, design of a single-propeller tilt-body MAV is largely affected by the following basic issues of the propulsion itself: propeller torque, *p*-factor, swirling slipstream, and gyroscopic moment. The propeller torque, which appears as a left-rolling tendency (the propeller is rotating clockwise as seen from inside the cockpit), is a serious drawback in a single-propeller-driven aircraft. Typically, the wingspan of aerobatic airplanes is greater than 1 m, which limits the maximum torque-roll rate by about 180 deg per second, allowing an inexperienced pilot to control the airplane. The maximum size for MAVs is 3–5-times smaller. Assuming that the torque-roll rate is inversely proportional to the cube of the wingspan, if the wingspan of an MAV decreases by a factor of 2, the torque-roll rate increases by a factor of 8. Thus, the torque-roll may become a driving factor in the design of the control system for VTOL MAVs.

Another negative effect in the single-propeller-driven aircraft is the *p* factor, which occurs as a result of the difference in angle of attack between the blades of a rotating propeller and causes a single-engine propeller aircraft to yaw. Deflecting of the rudder helps to maintain straight flight; however, as a consequence, the aircraft drag increases.

The effect of rotational airflow is inherent in a single-propeller propulsion system. The air rotating into a twisting helix around the fuselage presses against the vertical tail, causing the plane to yaw and roll. It also results in energy losses, reducing overall thrust efficiency of the propulsion.

In a tilt-body VTOL with contrarotating propellers, the second coaxial propeller is installed immediately behind the first one and rotates in the direction opposite to the rotating flow after the first one. The airflow coming out of a contrarotating propeller is symmetrical, without torque and side forces. The induced velocity behind the first propeller may increase the total thrust of the system in comparison with the flow of two propellers that stay apart.

From 1953–1955, Convair designed and successfully tested the XFY-1 Pogo aircraft with contrarotating propellers. Pogo successfully completed VTOL flights, but the project was cancelled at the completion of the test program. A jet tail-sitter Ryan X-13 Vertijet also completed VTOL flights in 1956–1957. Historically, large tilt-body tail-sitters have been envisioned for military use on both land and sea in situations disallowing airfields or for operating from limited space. Although short lived, tail-sitters paved the way for fixed-wing, jet-thrust-vectored aircraft, such as the Harrier. Among its problems, the pilot's uncomfortable accommodations were an important one, which, of course, is not important for unmanned air vehicles. Therefore, the tail-sitter designs with contrarotating motors and propellers are the focus of the current project.

Aerodynamic interaction of the wing with the propeller was studied by Prandtl [5] in a wind tunnel. In a series of tests lift, drag, and pitching moment on the wing and propeller thrust were measured. Increase of the drag was found to be noticeable when the wing was right behind the propeller. One of the issues of the interpretation of propeller–wing interaction is the right choice of reference speed. The increase of the speed behind the propeller was given as an explanation of the effect of drag increase, however, only a freestream speed was employed as a reference speed in the drag coefficient calculations [5], thus not taking into account propeller-induced velocity.

In general, a propeller generates a pulsating slipstream that can diminish performance of laminar wings with a tractor-propulsion installation. On the other hand, a pure pusher configuration is not an acceptable solution for VTOL aircraft that employ a propeller slipstream in aerodynamic controls.

In an earlier work [6], the laminar boundary layer was investigated on the NACA 27–212 airfoil in the presence of a freestream and propeller slipstream. It was found that the laminar-to-turbulent transition point is moving toward the leading edge of the wing, causing a significant increase in the drag.

One application of large unmanned air vehicles is for high-altitude surveillance. Aerodynamic design of this class of vehicles requires investigation of propeller–wing interaction at low Reynolds numbers but at high subsonic Mach numbers. Hot-film measurements were conducted in a study [7] to determine laminar, transitional, and turbulent boundary-layer states. It was concluded that a propeller-induced slipstream does not eliminate laminar separation bubbles. Note that test conditions corresponded to a Reynolds number of 5×10^5 and relatively low propeller rpm (revolutions per minute).

The effect of a propeller slipstream on the wing laminar boundary layer was investigated [8] with the help of hot-wire sensors. Measurements in the boundary layer on the wing surface showed the periodic change of the laminar velocity profile to turbulent and back at the same rate as of the propeller rotation.

Additional references on boundary-layer transition as a function of turbulence can be found elsewhere [9]. It is important to emphasize the fact that the previous studies [6–8] were performed for Reynolds numbers and thrust values relevant to large aircraft and high-speed flights. Also, these studies were concerned with a rotational flow behind a single propeller. Consequently, the results of the previous studies may or may not be applicable to the flow conditions pertaining to VTOL MAVs. Studies of slipstream disturbances and corresponding boundary-layer flows characteristic of low Reynolds number freestreams and slipstreams induced by small propellers with high RPMs are needed.

Since 2001, electric motors and lithium-polymer batteries, especially those mass-produced for cellular phones, have become an enabling technology for MAVs [10–12]. The components of electric propulsion systems and guidelines for their evaluation and selection have been presented in detail for MAV applications [13].

Effects of propulsive-induced flow on the aerodynamic characteristics of MAVs in tractor configurations with a wing right behind a propeller have been studied experimentally [14]. A significant increase in lift coefficients (referred to a dynamic pressure in the freestream) and the delayed stall phenomenon was reported, especially when it comes to low-speed flight performance. The delayed stall seen with the induced propeller flow would allow a MAV to attain a higher angle of attack before aerodynamic stall, and, hence, attain a higher lift coefficient and slower flight speed than what would be thought possible just from wing aerodynamics alone. On the other hand, it was noted that the lift-to-drag ratios for nearly all angles of attack were greater for the wing-only tests. It appears that even though the lift coefficients are increased due to the induced flow, the subsequent increase in the drag coefficient, both from the added lift and the parasite drag of the motor–propeller combination, increases the drag by a more substantial amount, leading to the decrease in the lift-to-drag ratios. To the contrary, investigations of a biplane configuration showed that the pusher arrangement of the propeller improves the overall performance of the vehicle [15].

VTOL capabilities pose difficult problems for a fixed-wing MAV design. VTOL MAVs flying at low Reynolds numbers will have relatively large propeller sizes and larger control surfaces and throws. Owing to the complexity of the propeller–wing interactions, no design methods exist for sizing these airplanes. Therefore, in the present study, the aerodynamics of VTOL MAVs will be studied through wind-tunnel measurements on a propulsion system consisting of two contrarotating motors and propellers, wing, and wing with propulsion system. As evident from the preceding discussion, the tilt-body concept with contrarotating propellers represents a workable solution for the reduction or elimination of the negative effects of other concepts. In the present study, a tilt-body VTOL MAV was designed based on previous successful designs [3,4].

II. Models and Methods

A. Propulsion System for VTOL MAVs

The propulsion system shown in Fig. 2 consists of two pairs of coaxial contrarotating motors and propellers. Each propeller is powered by a separate motor, rotating in opposite directions. This propulsion system was assembled by using off-the-shelf brushless outrunners MP Jet AC 22/4-60D. The motors are joined at their stator backplates. The outrunner motors have sufficient space inside the stators to allow a cross shaft through both motors, as shown in Fig. 2. Propeller 1 is attached to one end of the cross shaft and the other end is fixed to the rotor case of motor 1. The rotor of motor 2 was modified with an extended shaft, which also houses two bearings supporting the cross shaft. The motors have a diameter of 27 mm, and the total length of the propulsion is 60 mm. In this work, the motors are regulated by an electric speed controller Phoenix-25 providing the same number of rpm to both motors. The effect of unequal rpm may be of interest for future studies, especially with regard to possible roll controlling of a vehicle through the differential rpm.

Two arrangements of the propellers with respect to the motors were analyzed: tractor and pusher. In a tractor configuration, propellers are attached to the motors such that the thrust force is generated in the positive direction of the s axis, and the propeller slipstream hits the motors. For the pusher configuration, shown in Fig. 2, propellers were flipped 180 deg, and the polarity of the electric power was set to opposite to that used previously. Propellers used are APC with a 140-mm diameter (radius $R = 70$ mm) and 114-mm pitch. The distance between propellers is 17 mm.

B. Wing Design

The Zimmerman planform wing with a 254-mm wingspan, 169-mm root chord, and aspect ratio of 1.91 is studied in this work. The S5010-TOP24C-REF airfoil [16] was used in designing the wing, with a maximum camber of 3% located at $0.24c$ and an inverse camber of 1% at $0.85c$. The wing area is 335 cm^2. The wing geometry, presented in Fig. 3, was generated using SolidWorks$^{\mathrm{TM}}$ as described in [17]. It is stiffened by a plywood rib along the root chord, as shown in Fig. 4. The rib provides stiffness to a very thin wing (wing thickness is 0.5 mm) and, therefore, it is considered as a part of the structure. The mold was manufactured employing a 3D InVision Si2 printer. No fuselage or controls were attached to the wing studied in this work.

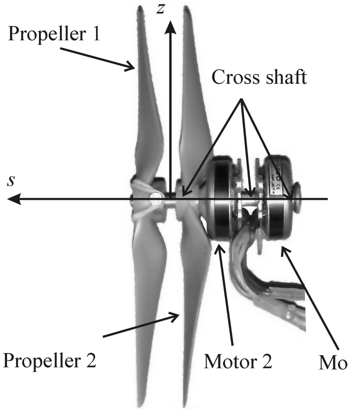

Fig. 2 Propulsion system of two coaxial contrarotating motors and propellers.

C. Motor Testing Bench and Hot-Wire Measuring System

The motor testing bench in the Institut Supérieur de l’Aéronautique et de l’Espace (ISAE) Propulsion Lab is used for the evaluation of small electric motor propulsion. It measures rpm, current, thrust, and torque, with the voltage being held constant. Two load cells provide thrust and torque values. Calibration of the devices was done by applying a calibrated mass to the sensors. The resolution for the thrust force was 0.005 N and for the torque 0.2 N mm.

A hot-wire measuring system has been used to investigate the velocity profile of propeller flow. The sensor is a 2-D hot wire, model 1241-20 from TSI, Inc. It allows two normal velocity components to be measured, but in this study only axial-flow velocity was used. This sensor is managed by an IFA 300 constant-temperature anemometer system from TSI, Inc. The two electric signals resulting from this acquisition system are translated into two velocity values using a MATLAB® routine on the acquisition computer. Calibration of the

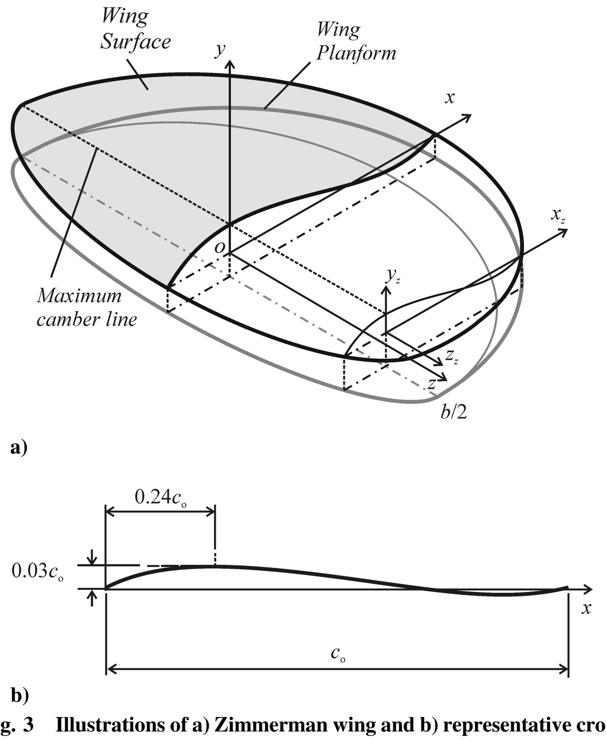

Fig. 3 Illustrations of a) Zimmerman wing and b) representative cross section.

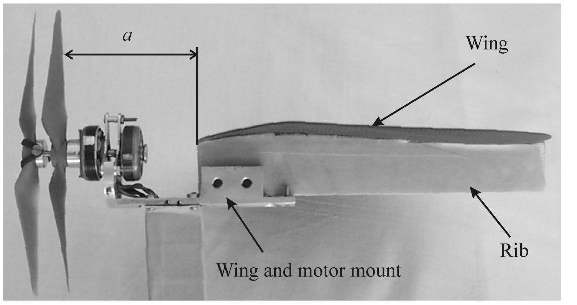

Fig. 4 Experimental arrangements for testing of a wing with a motor.

acquisition system is achieved in the wind-tunnel test section. A 2-D map of each wire voltage is generated using wind speed and sensor angle as the two input parameters. Discrete values of wind speed from 0 to 30 m/s are set with a step of 1 m/s. For each wind speed, the sensor angle is set from −45 to 45 deg, with a 1-deg step. The resulting 2-D map for one wire is a continuous surface. A voltage value for this wire will result in a line in the (wind speed, angle) plane. Given a voltage for each wire, the intersection of the resulting lines will lead to a single point equivalent to unique speed and angle values. This calibration method provides better accuracy for the whole measurement range than the usual polynomial formula. The wind speed measured during calibration is provided from a calibrated Pitot tube, whose accuracy is better than 0.1 m/s for the speed range obtained from the propeller flow. The angle is measured by a digital potentiometer, which has a precision of 0.01 deg.

Experimental arrangements for testing a wing with a motor are presented in Fig. 4. The distance from propeller 2 to the leading edge of the wing was set at $a = 65$ mm. For testing of the motor only, the wing was removed and testing was conducted using the same fixture.

D. Wind-Tunnel Facility

The ISAE low-speed wind tunnel is a closed-loop wind tunnel where the test section has a 0.45 × 0.45 m cross section and is 0.7 m long. The contraction ratio is 6.2 and the turbulence level is 1%. Speeds from 2 to 30 m/s can be obtained with a standard deviation below 0.2 m/s.

The balance measures all the aerodynamic components except for the side force. It is composed of 6 single-ended load cells. Three struts, each linked to 2 cells, go through the test section floor and connect to the test model. Balance calibration is achieved by computing the calibration slope of each cell using calibrated weights. The resolution for forces is less than 0.004 N.

A calibration of the wind tunnel and the balance was performed before each test series. Using calibration measurements and the small-sample method [18], the uncertainty intervals in aerodynamic coefficients were determined. Standard deviations of aerodynamic coefficients were estimated. Solid blockage, wake blockage, and streamlined curvature corrections were estimated based on the methods described in [19].

III. Evaluation of Propulsion System

A. Motor Static Testing

The performance during hover and vertical climb of a VTOL aircraft is a driving factor in the takeoff weight determination and power selection. Because these flight conditions are characterized by a relatively low speed, knowledge of the static thrust at zero freestream velocity becomes very important. Other parameters affecting the design include torque, rpm, and power requirements. Several propulsion systems were evaluated on the motor testing bench. The tests were conducted for a constant voltage from 6 to 11 V, with a step of 0.5 V. With the voltage set, the motors were started and measurements were taken at the control signal to the motors in terms of PWM (pulse width modulation), which varied from 50 to 80%, where the former corresponds to 1.5 ms and latter to 1.8 ms. Both tractor and pusher arrangements of contrarotating propulsion were investigated, as well as a conventional single motor–propeller setup.

In Fig. 5, the variation of thrust and torque with PWM is presented for the tractor at 11 V. The thrust force increases linearly with PWM and reaches a maximum at 3.42 N and 12,000 rpm. This thrust is 1.9 times greater than the thrust generated by a single-propeller motor under the same voltage and PWM. Thus, there is a small loss of thrust in the contrarotating system compared with a single-propeller motor, which can be explained by the nonoptimal propellers selected for the present study. Note that the linear relationship simplifies thrust control in an automatic system.

The maximum torque in this test was 0.42 N-cm, which is also the maximum torque measured in all tests conducted for contrarotating systems. As expected, this torque was about 10 times lower in comparison with a torque measured on a single-propeller-motor system. This feature of the contrarotating propulsion significantly simplifies controls for VTOL aircraft, and it is a major advantage of the presented propulsion system.

Figure 6 shows the static thrust generated by both pusher and tractor propulsion systems as a function of electric power input. The presented data provide estimates of the power required for hovering flight and can be used for battery selection. As evident from Fig. 6, the pusher propulsion generates 20–23% more thrust force than the tractor for the same input power. It directly affects the takeoff weight and flight performance of the vehicle in hover and climb. In the tractor configuration, the motor is placed right behind the propellers and, therefore, creates a significant parasite drag. Hence, the shape optimization of the motor mount and fuselage is another important area of research for aerodynamic design at low Reynolds numbers.

B. Slipstream Velocity Profiles

A hot-wire system was used for measuring air-velocity profiles in a slipstream behind the propellers. A propulsion system was still sitting on the motor testing bench, whereas the hot-wire probe was mounted on its top, allowing simultaneous measurements of air velocity and thrust, power input, voltage, etc. The testing was conducted at a constant voltage of 8.5 V and the PWM was set to hold the thrust constant. However, in the course of the tests, a 3–5% drift of the thrust was observed and the PWM was manually adjusted to the desired thrust.

The measurements were conducted at four sections located at distances $s = 35$, 70, 130, and −70 mm (Fig. 2), respectively, with the first three sections referring to the pusher arrangement and the last section to the tractor. For each section, the air-velocity component in the s direction was measured at points along the z coordinate from 0

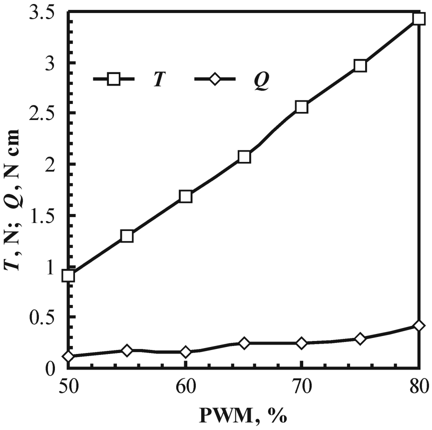

Fig. 5 Variation of thrust and torque with PWM.

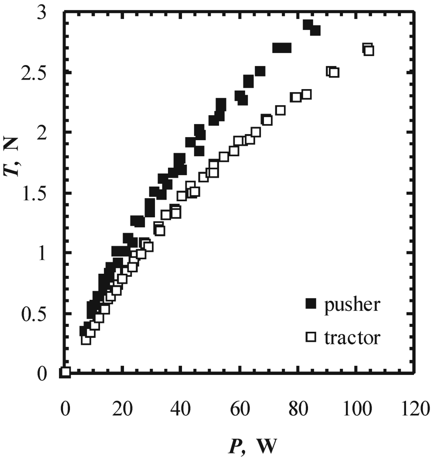

Fig. 6 Thrust of the propulsion system as a function of input power.

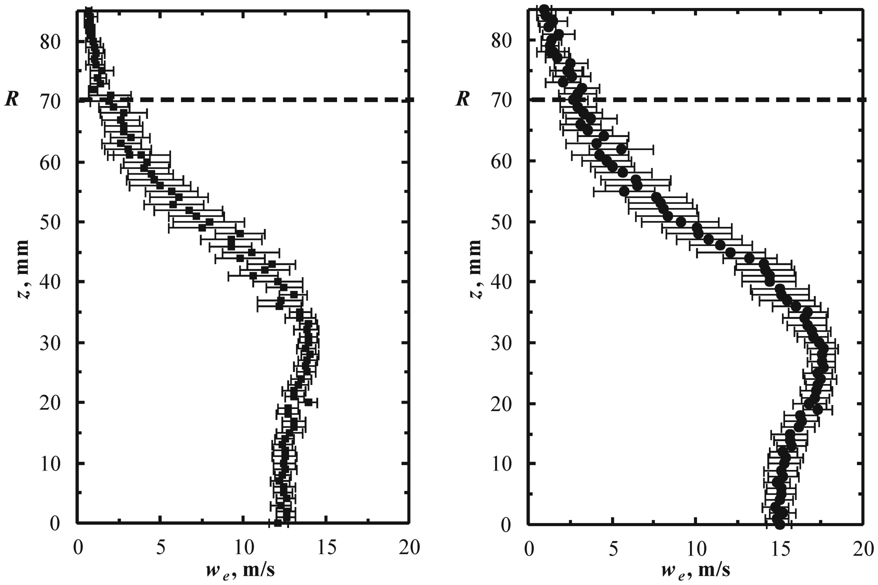

Fig. 7 Experimental velocity profiles at section $s = 130$ mm at $T = 1.47$ N (left) and $T = 2.45$ N (right) for a pusher arrangement.

to a maximum distance $R_m = 85$ mm, with a step of 1 mm. The propeller's radius R corresponds to $z = 70$ mm.

Air-velocity distribution in the pusher propeller slipstream can be seen in Fig. 7 for two values of thrust: $T = 1.47$ and $T = 2.45$ N. The plots exhibit a single-hump shape, with the maximum of velocity near the point $z = 0.5R$. With z increases beyond the propeller radius, the velocity asymptotically approaches zero. The local decrease of the air velocity (by about 15%) closer to the axis of rotation may be caused by the propeller's hub and the interference of the propellers with the motors. The fluctuations in velocities in terms of a standard deviation were determined and error bars plotted in Fig. 7. They are indicative of nonstationary, pulsating flow behind the propellers. The increase in size of the error bars illustrates the presence of vortices in the area near the propeller tips. Also, larger pulsations are noticed for higher thrust force.

Air-velocity profiles in Fig. 8 are shown for three sections at the same thrust force. This figure shows the change in the profile: the farther they are from the propeller, the more uniform they become.

Figure 9 illustrates velocity profiles at sections placed at the same distance, $|s| = 70$ mm, from the propeller in the pusher and tractor arrangements. In fact, for the tractor arrangement, the velocity is measured right behind the aft motor. The lower average velocity and significant decrease of velocity in the core of the slipstream found in the tractor arrangement are mostly due to the parasite drag caused by the motors and to some degree by the motor mount. These results also explain the overall decrease of the thrust force for the tractor arrangement in comparison to the pusher arrangement, as evident from Fig. 6.

Now, using measured air-velocity data, the values of thrust and induced power can be determined. Consider a cylindrical control volume around the propeller. It is assumed to be very large so that the transport of mass and momentum through its walls is negligible, except through the side circular wall of radius $R_m = 85$ mm (of area, S_S) placed in the propeller slipstream at a distance s from the propeller. Applying the momentum and energy theorems, the static thrust is found from

$$T_s = \rho \int_{S_S} V^2 \, \mathrm{d}S \tag{1}$$

and the power induced into the flow is

$$P_{\mathrm{ind}} = \frac{\rho}{2} \int_{S_S} V^3 \, \mathrm{d}S \tag{2}$$

Assuming that the air velocity remains constant in the azimuthal direction, the calculations of T_s and P_{ind} were conducted by substituting hot-wire data into Eqs. (1) and (2). In addition, the figure of merit $f_M = P_{\mathrm{ind}}/P$ was computed.

Numerical results obtained through the use of air-velocity data for sections $s = 70$ mm (for pusher) and $s = -70$ mm (for tractor) are presented in Table 1 for a nominal thrust of 1.47 N. Obtained T_s values differ from the nominal by about 5%, which is a good agreement when one takes into account the drift (mentioned earlier) of the thrust during these tests. As expected, for the same nominal thrust, the pusher generates higher induced power and has a higher figure of merit.

The obtained results will be used here for verification of the propeller momentum theory for slipstream velocity predictions. By following derivations from [1], the propeller-induced velocity at a distance s from the propeller disk is given by

$$w(s) = w(0)\left[1 + \frac{s/R}{\sqrt{1 + (s/R)^2}}\right] \tag{3}$$

$$w(0) = 0.5\left[\sqrt{V_0^2 + \frac{2T}{\rho \pi R^2}} - V_0\right] \tag{4}$$

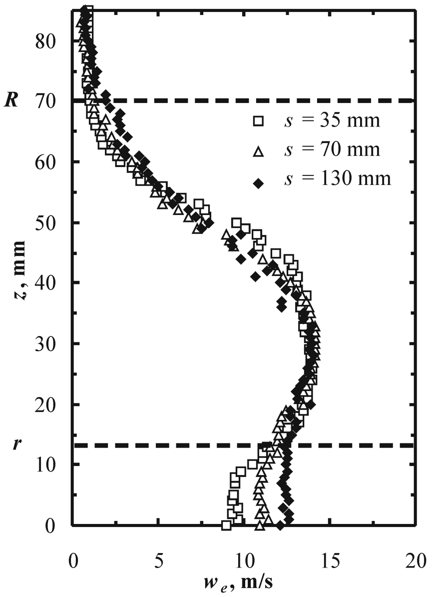

Fig. 8 Comparison of air-velocity profiles for three sections in a pusher at $T = 1.47$ N.

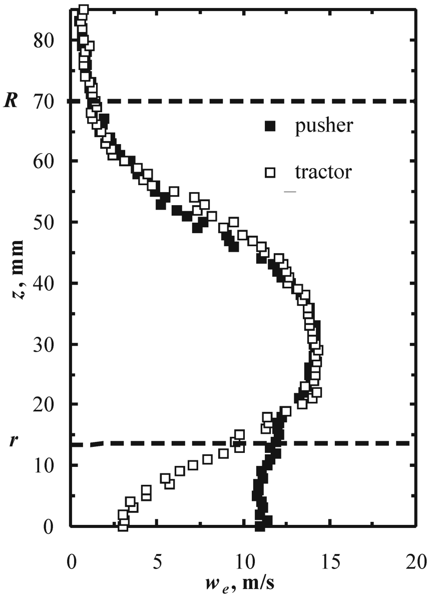

Fig. 9 Pusher vs tractor comparisons for air-velocity profiles at $|s| = 70$ mm, $T = 1.47$ N.

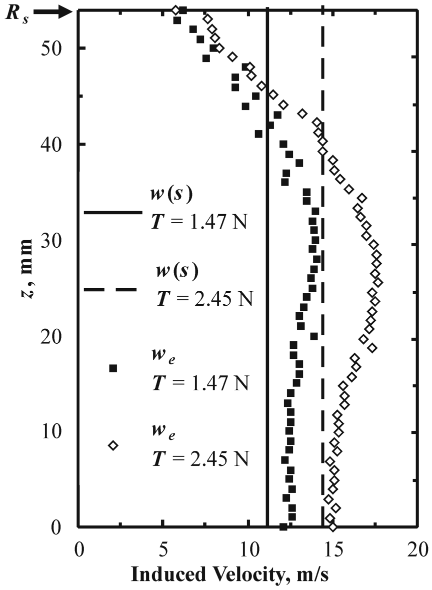

Fig. 10 Comparison of experimental results against propeller momentum theory at $s = 70$ mm.

where V_0 is the freestream velocity. The radius of the stream tube behind the propeller, R_s, can be found from the equation

$$R_s = R\sqrt{\frac{w(0)}{w(s)}} \tag{5}$$

The velocity and the radius of the stream tube were computed for the section $s = 70$ mm for two values of the static thrust. The numerical results obtained with the help of Eq. (3) are shown in Fig. 10, together with experimental data w_e. Overall, their matching is satisfactory, and, therefore, the propeller momentum theory can be recommended for air-velocity predictions to be used in the aerodynamic analysis and sizing of the wing, fuselage, and control surfaces of VTOL MAVs.

IV. Wind-Tunnel Testing

A. Wing-Only Tests

Experimental measurements in wind tunnels at low Reynolds numbers become difficult because aerodynamic forces are small at low angles of attack, requiring high accuracy and sensitivity of measuring facilities. For these reasons, the validation of available aerodynamic data for wings used in the current designs is an important task itself in the development of a reliable database on MAVs.

A series of wind-tunnel tests was conducted on wind-tunnel models of the Zimmerman wing with 3 and 9% camber [17]. These tests were done without a motor or fuselage to determine the exact role that camber plays in the aerodynamics of the vehicles. In the present study, the same 3% model that was previously tested in the University of Arizona wind tunnel [17] was tested in the ISAE wind tunnel.

The tests were conducted for two values of velocities 5 and 10 m/s corresponding to mean aerodynamic chord Reynolds numbers of 5×10^4 and 10^5, respectively. The results are presented in Figs. 11 and 12 for the lift and drag coefficients, respectively. It can be seen from the plots that lift coefficients are in reasonable agreement for both moderate and low angles of attack. The present side-by-side comparison indicates that stall is predicted at slightly different values of the angle of attack. This might be due to differences in the turbulence level in both wind tunnels.

For the drag coefficients, there is a reasonable agreement of the results at the moderate angles of attack, which becomes worse when α approaches angles corresponding to the maximum lift coefficient.

The zero-lift drag coefficient, C_{D_0}, is especially interesting in designing MAVs for hovering and vertical flight conditions. For the Reynolds number 10^5, the C_{D_0} coefficient obtained in ISAE is 0.025, which is higher than the value of 0.02 from the University of Arizona tests. Note that for very small α, the magnitude of the measured drag becomes smaller and has increased scatter for both testing facilities.

Table 1 Thrust, power, and figure of merit for propulsion systems

Propeller arrangement	T_s, N	P, W	P_{ind}, W	f_M
Pusher	1.43	42.5	8.62	0.203
Tractor	1.55	45.0	8.20	0.182

B. Motor Tests in Wind Tunnel

A contrarotating propulsion system in a tractor arrangement was mounted to the top of the struts in the ISAE wind-tunnel test section. With the power set to on and the motor running, the tunnel flow was started and thrust measurements were taken at tunnel velocities ranging from 0 to 15 m/s. The tests were conducted with 11 V supplied to the motors and with PWM varying from 55 to 70%, so that an accurate model of the thrust behavior of the propulsion was obtained. A difference between the test-bench (Fig. 5) and wind-tunnel static thrust data was noticed that can be attributed to the different drags of the struts on the test bench and in the wind tunnel.

The experimental results are presented in Fig. 13 for PWM = 55, 60, 65, and 70%, and for average freestream velocity $V_0 = 3$, 4.5, 9.25, and 13.7 m/s. As expected, the thrust varies linearly with PWM, and it decreases as freestream velocity increases.

C. Determination of Wing Drag Because of Freestream and Propeller Slipstream

Hover and vertical flight efficiency is one of the single-most important qualities that VTOL MAVs must exhibit. It affects the maximum required thrust and power and determines the endurance for loitering over a target area. This part of the study will focus on the determination of drag forces at near-zero angles of attack in the presence of both freestream flow and propeller-induced flow.

This series of tests was conducted in the ISAE wind tunnel. The wind-tunnel model shown in Fig. 4 consists of contrarotating propulsion and a Zimmerman wing connected through a common mount fixture. The motors were installed such that the thrust line is collinear with the root chord line. The motors were set at 11 V and

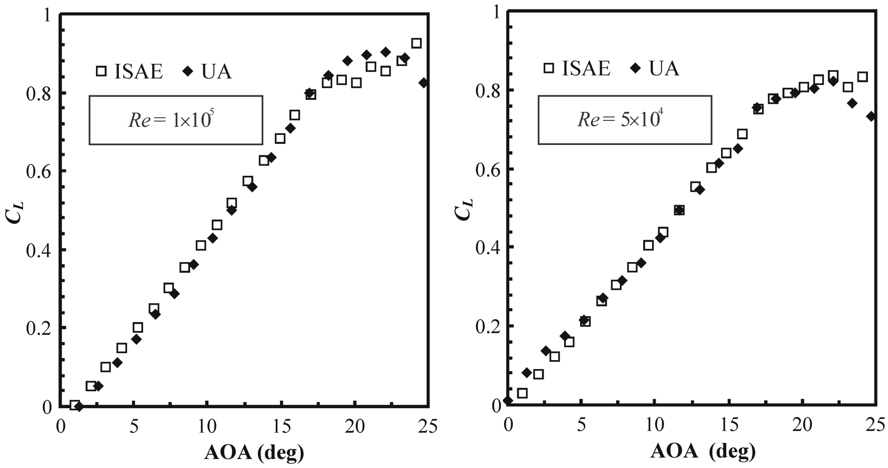

Fig. 11 Lift coefficient variation with angle of attack (AOA).

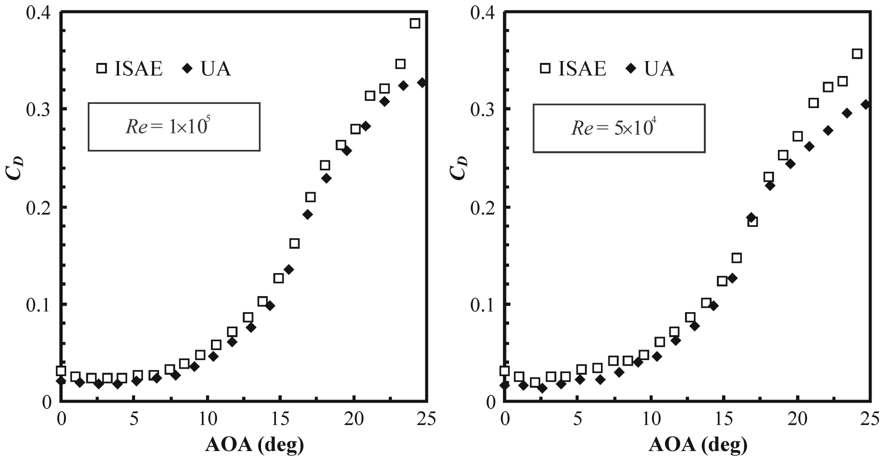

Fig. 12 Drag coefficient variation with angle of attack (AOA).

PWM varied from 55 to 70%. The freestream velocity V_0 ranged from 0 to 15 m/s.

For a given combination of PWM and V_0, the wind-tunnel balance measures the total force F_{total}, which is the sum of the thrust force generated by a propeller and the drag force on the wing. This force corresponds to a zero-lift angle of attack. From the motor tests described in the previous section, the amount of thrust T produced at each freestream velocity V_0 is known. The drag on the wing D_0 is generated from two mixing airflows: freestream and propeller slipstream. Assuming that there is no upstream influence from the wing on the propeller and, because the motor and wing were mounted on the same fixture as in the motor-only tests, the drag force can be determined as $D_0 = |F_{\text{total}} - T|$ and is presented in Fig. 14. For clarification, the total force F_{total} is smaller in magnitude than the propulsive thrust T and also, because of the test procedure, the zero-lift drag force D_0 has no fixture or strut effects on it. Also, the magnitude of D_0 is much smaller than both F_{total} and T. As expected, drag force D_0 increases as PWM with a corresponding thrust force T increases.

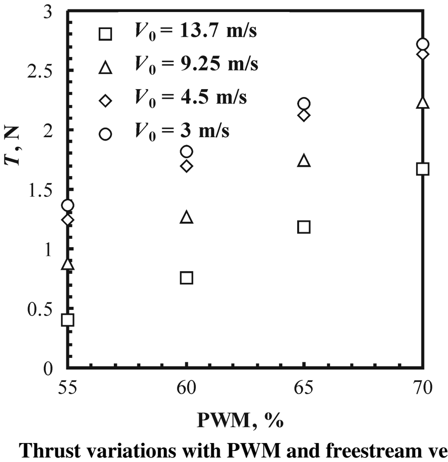

Fig. 13 Thrust variations with PWM and freestream velocity.

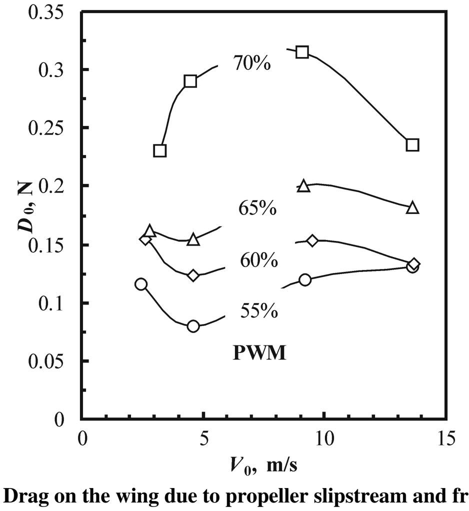

Fig. 14 Drag on the wing due to propeller slipstream and freestream.

D. Zero-Lift Drag Model

A classical propeller momentum theory is applied in the present study for modeling of the zero-lift drag of a wing. The assumptions used in the development of the propeller theory can be found elsewhere [1], but one important approximation is that a sharp-stream tube is formed behind the propeller. In the present study, overall, a satisfactory match of theoretical results and experimental data was found (section III.B). However, it can be seen in Figs. 7–9 that the edge of the slipstream is very difficult to determine. Hence, a stream tube in the propeller momentum theory should be considered as a first approximation for the flow.

The stream tube separates the flow passing through the propeller from the rest of the airflow, and the tube's radius can be found from Eq. (5). As a result, a part of the wing area S_p (see Fig. 15) is submerged into the propeller slipstream, the freestream of the velocity V_0 enters the rest of the wing area $S_0 - S_p$. The slipstream velocity at distance s from the propeller $V_P(s)$ is constant over a cross section of the stream tube and equal to the sum

$$V_P(s) = V_0 + w(s) \tag{6}$$

where the induced velocity $w(s)$ is given by Eq. (3).

Based on this flow model, the zero-lift drag produced by a freestream and slipstream over the wing can be presented as the following sum:

$$D_0 = D_{V_0} + D_{V_P} \tag{7}$$

Here, the zero-lift drag occurring on the part of the wing covered by a freestream flow only is

$$D_{V_0} = 0.5\rho C_{D_0} V_0^2 (S_0 - S_p) \tag{8}$$

The zero-lift drag on the part of the wing submerged into a stream tube can be written as

$$D_{V_P} = 0.5\rho C_{D_P} \int_{S_p} V_P^2(s)\, \mathrm{d}S_p \tag{9}$$

where C_{D_P} is the zero-lift drag coefficient for this part of the wing. Rearranging Eqs. (7–9), a formula for the drag coefficient is derived as

$$C_{D_P} = \frac{D_0 - 0.5\rho C_{D_0} V_0^2 (S_0 - S_p)}{0.5\rho \int_{S_p} V_P^2(s)\, \mathrm{d}S_p} \tag{10}$$

This formula is also valid when either propeller-induced velocity or freestream velocity is zero.

Based on the results of the wing-only tests, the average value of 0.025 is chosen for the coefficient C_{D_0}. Using experimental data for the drag force D_0 (Fig. 14) the drag coefficient C_{D_P} was computed from Eq. (10) and results presented in Table 2. The drag coefficient increases with PWM increases, except for one point at $V_0 = 3$ m/s. The effect of freestream velocity in the presence of a running propeller is less obvious, because it influences the induced velocity through Eq. (3). It is seen, however, that as V_0 increases the effect of the propeller slipstream on C_{D_P} decreases.

Table 2 Zero-lift drag coefficients C_{D_P}

	V_0, m/s			
PWM, %	3	4.5	9.25	13.7
55	0.0828	0.0530	0.0585	0.0396
60	0.0838	0.0631	0.0618	0.0347
65	0.0717	0.0653	0.0708	0.0466
70	0.0835	0.1027	0.0980	0.0553

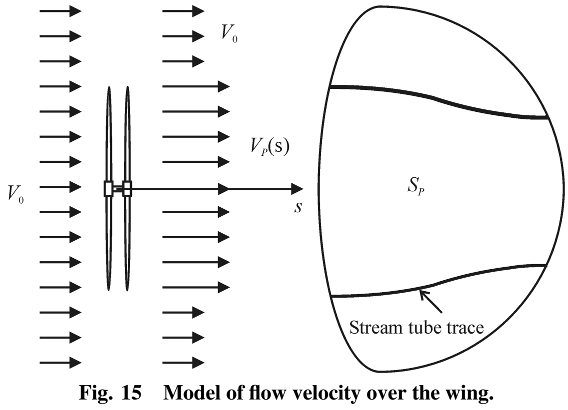

Fig. 15 Model of flow velocity over the wing.

Using thrust data presented in Fig. 13, the induced velocity $w(0)$ was computed from Eq. (4) and the drag coefficient C_{D_P} is presented in Fig. 16 as a function of $w(0)$. These results demonstrate that the slipstream behind the propeller has a profound negative effect on the drag of the wing. For low-power and low-$w(0)$ conditions, the drag coefficient C_{D_P} approaches the $C_{D_0} = 0.025$ obtained for the wing-only test. The drag coefficient increases by about 4-times, with induced speed increasing from 0 to 7.5 m/ sec. Although the data are scattered, the correlation between drag coefficient and induced velocity is meaningful and can be presented for the entire dataset by the quadratic regression

$$C_{D_P} = -0.0009w^2(0) + 0.0147w(0) + 0.0237 \tag{11}$$

represented by a solid line in Fig. 16.

V. Designing a VTOL MAV Prototype

The obtained results can be used for designing VTOL MAVs with vertical flight requirements. Even though this procedure gives only one design point, it is an utmost important one for the selection of the propulsion system and power source. For the steady vertical flight of an aircraft with a takeoff weight of W, the balance of forces in a vertical direction can be written as

$$T - W - D_0 = 0 \tag{12}$$

By combining Eqs. (7–9) and (11), the thrust required for the vertical flight at a speed V_0 can be found from

$$T - W - 0.5\rho\left[C_{D_0} V_0^2 (S_0 - S_p) + (-0.0009w^2(0) + 0.0147w(0) + 0.0237)\int_{S_p} V_P^2(s)\, \mathrm{d}S_p\right] = 0 \tag{13}$$

The first VTOL MAV prototype (Fig. 17) has been designed based on the propulsion system described in this paper. The aircraft is equipped with a flat plate wing of Zimmerman planform. It has a takeoff weight of $W = 1.76$ N, wingspan of 30 cm, and wing area of

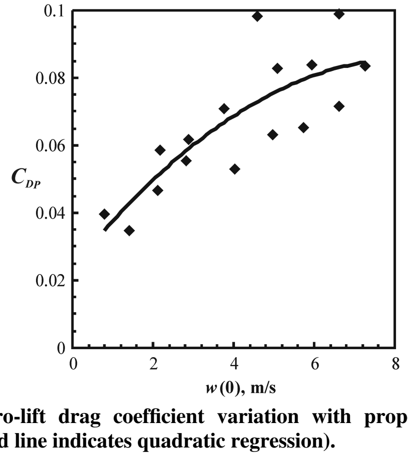

Fig. 16 Zero-lift drag coefficient variation with propeller-induced velocity (solid line indicates quadratic regression).

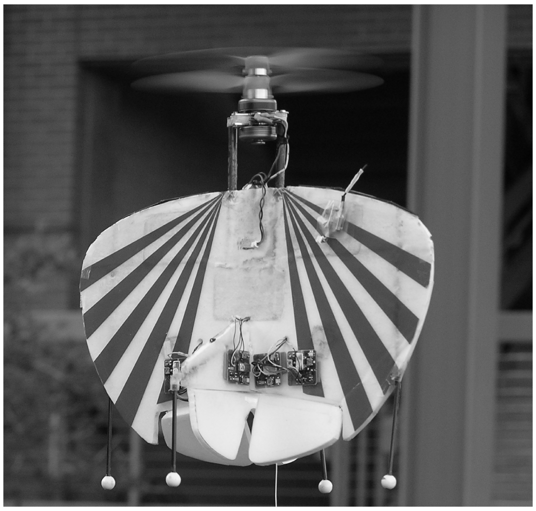

Fig. 17 VTOL MAV in hover.

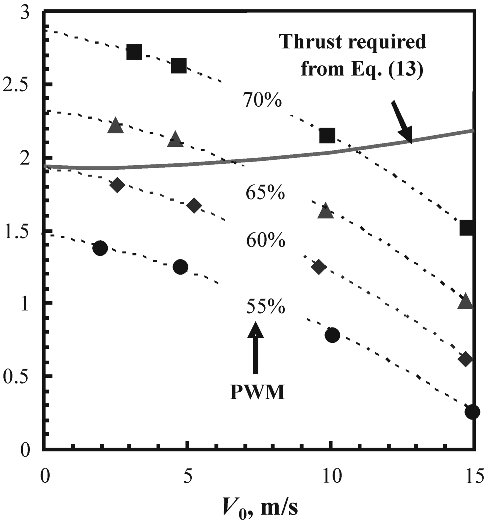

Fig. 18 Variations of available and required thrust with freestream speed (symbols indicate experimental data points, dashed lines indicate quadratic approximations).

$S_0 = 488\ \mathrm{cm}^2$. Using these data, the thrust required to climb vertically with a rate of climb V_0 was obtained numerically from Eq. (13) and plotted in Fig. 18. It can be seen that as the rate of climb increases, the required thrust is slightly increased, with a maximum of 2.3 N. From a comparison of thrust available and required (Fig. 18), the thrust available from the current propulsion will provide a steady vertical flight in the range of climb rates 0–10 m/s, with PWM in the range of 60–70%.

As can be seen from Fig. 6, about 80 W of maximum power is needed to support the flight mission characterized by the maximum required thrust of 2.3 N. To satisfy this requirement, a 3-cell lithium-polymer battery of 740 mAh capacity was selected as an onboard power source.

Two fins with a total area of $67\ \mathrm{cm}^2$ provide stabilization of the aircraft in roll and yaw. A rudder consisting of two connected sections (total area of $50\ \mathrm{cm}^2$) is attached to fins. Two elevons (total area $60\ \mathrm{cm}^2$) control the vehicle in pitch and yaw.

Test flights were conducted with this vehicle demonstrating a hover, sustained vertical climbs, and transition to and from a level flight. Remember that the PWM required for a hover is 60% (see Fig. 18). During flight tests, the throttle on the RC transmitter was observed at a position corresponding to PWM = 62–66%. Note that the pilot was continuously adjusting the controls through a set of gyrometers to keep the aircraft stable. With this setting, the MAV demonstrated a sustained hover. Thus, flight tests proved the feasibility of the design concept and showed that the developed model and data are sufficient for designing VTOL MAVs.

VI. Conclusions

In the present study, a tilt-body, tail-sitter concept for VTOL MAVs was analyzed, and a design was proposed based on a contrarotating propeller-motor electric propulsion system. As evident from the discussion, this design represents a workable solution for the reduction or elimination of the negative effects of other concepts.

The evaluation of propulsion was conducted for two propeller arrangements: pusher and tractor. Static thrust measurements, as well as measurements of rpm, power, and torque, were conducted on a motor testing bench. A small loss of thrust in the contrarotating system was found compared with a single-propeller motor. The maximum torque for the contrarotating system was about 10 times lower than a torque measured on a single-propeller-motor system. The pusher arrangement of the propeller generates 20–23% more thrust force than the tractor for the same input power. In the tractor configuration, the motor is placed right behind the propellers, creating a significant parasite drag. Hence, the shape optimization of a motor mount and fuselage is another important area of research for aerodynamic design at low Reynolds numbers.

A hot-wire system was used for measuring air-velocity profiles in a slipstream behind propellers. The fluctuations in velocities in terms of a standard deviation were determined. They are indicative of nonstationary, pulsating flow behind the propellers. For the tractor arrangement, lower average velocity and a significant decrease of velocity in the slipstream core are mostly due to the parasite drag caused by the motors' placement right behind the propellers. These results also explain the overall decrease of thrust force for the tractor arrangement in comparison with the pusher arrangement.

In the present study, the same 3% Zimmerman wing that was previously tested in the University of Arizona wind tunnel was tested in the ISAE wind tunnel. The results for the lift and drag coefficients are in reasonable agreement for both high and low angles of attack.

The aerodynamics of a wing–propeller combination was studied through wind-tunnel measurements. Results clearly demonstrate that for a given range of propeller thrust, the slipstream behind the propeller has a profound negative effect on the drag of the wing for zero-lift angles of attack. The drag on the wing is generated from two mixing airflows: freestream and propeller slipstream. A drag force model based on the classical propeller momentum theory is introduced in the present study, and a formula for the drag coefficient for the wing in the presence of a freestream and slipstream is derived.

Using obtained experimental data for drag forces, the zero-lift drag coefficient was computed as a function of the propeller-induced velocity. The zero-lift drag coefficient increases 4 times, with induced speed increasing from 0 to 7.5 m/s.

The results obtained in the present study were realized in a design of a VTOL MAV prototype that was successfully flight tested.

Acknowledgments

This project represents collaborative efforts of the University of Arizona and Institut Supérieur de l'Aéronautique et de l'Espace toward the development of vertical take off and landing micro air vehicle technologies. It was sponsored by grants to the University of Arizona from the U.S. Air Force Research Laboratory and Eglin Air Force Base (Program Manager Gregg Abate) and to Institut Supérieur de l'Aéronautique et de l'Espace by the European Office of Aerospace Research and Development, London (Program Manager Surya Surampudi). The authors also would like to thank the other members of the Micro Air Vehicle Project at both universities for their contributions to this work: Bill Silin, David Addai, and Chinnapat Thipyopas. Sergey Shkarayev would like to thank the Institut Supérieur de l'Aéronautique et de l'Espace team for their support of research on vertical take off and landing micro air vehicles during his visiting appointment there.

References

[1] McCormick, B. W., Jr., *Aerodynamics of V/STOL Flight*, Dover, New York, 1999.

[2] Kohlman, D., *Introduction to V/STOL Airplanes*, Iowa State Univ. Press, Ames, IA, 1981.

[3] Krashanitsa, R., Platanitis, G., Silin, D., and Shkarayev, S., "Autopilot Integration into Micro Air Vehicles," *Introduction to the Design of Fixed-Wing Micro Aerial Vehicles*, edited by T. J. Mueller, J. C. Kellogg, P. G. Ifju, and S. V. Shkarayev, AIAA, Reston, VA, 2007, pp. 109–149, Chap. 3.

[4] Bataille, B., Poinsot, D., Thipyopas, C., and Moschetta, J. M., "Fixed-Wing Micro Air Vehicles with Hovering Capabilities," *Symposium on Platform Innovations and System Integration for Unmanned Air, Land and Sea Vehicles*, RTO-MP-AVT-146, NATO, May 2007, Paper 38.

[5] Prandtl, L., "Mutual Influence of Wings and Propeller," NACA TN 74, Sec. 6, Dec. 1921, Chap. 4.

[6] Hood, M. J., and Gaydos, M. E., "Effects of Propellers and Vibration on the Extent of Laminar Flow on the NACA 27-212 Airfoil," NACA ACR (WR L-784), 1939.

[7] Elsaadawy, E. A., and Britcher, C. P., "Effect of Propeller Slipstream on Heat-Exchanger Installations at Low Reynolds Number," *Journal of Aircraft*, Vol. 40, No. 4, 2003, pp. 751–758.

[8] Miley, S. J., Howard, R. M., and Holmes, B. J., "Wing Laminar Boundary Layer in the Presence of a Propeller Slipstream," *Journal of Aircraft*, Vol. 25, No. 7, 1988, pp. 606–611.
doi:10.2514/3.45630

[9] Hoerner, S. F., *Fluid-Dynamic Drag*, Hoerner Fluid Dynamics, Brick Town, NJ, 1965.

[10] *Micro Air Vehicle Design Papers, 6th International MAV Competition*, Brigham Young Univ., Provo, UT, Apr. 2002.

[11] *Micro Air Vehicle Design Papers, 7th International MAV Competition*, Univ. of Florida, Gainesville, FL, Apr. 2003.

[12] *Micro Air Vehicle Design Papers, 8th International MAV Competition*, Univ. of Arizona, Tucson, AZ, Apr. 2004.

[13] Mueller, T. J., Torres, G. E., and Srull, D. W., *Elements of Aerodynamics, Propulsion, and Design, Introduction to the Design of Fixed-Wing Micro Aerial Vehicles*, edited by T. J. Mueller, J. C. Kellogg, P. G. Ifju, and S. V. Shkarayev, AIAA, Reston, VA, 2006, Chap. 2, pp. 39–107.

[14] Null, W., Noseck, A., and Shkarayev, S., "Effects of Propulsive-Induced Flow on the Aerodynamics of Micro Air Vehicles," 23rd AIAA Applied Aerodynamics Conference, Toronto, AIAA Paper 2005-4626, 2005.

[15] Moschetta, J. M., and Thipyopas, C., "Aerodynamic Performance of a Biplane Micro Air Vehicle," *Journal of Aircraft*, Vol. 44, No. 1, 2007, pp. 291–299.
doi:10.2514/1.23286

[16] Null, W., and Shkarayev, S., "Effect of Camber on the Aerodynamics of Adaptive Wing Micro Air Vehicles," *Journal of Aircraft*, Vol. 42, No. 6, 2005, pp. 1537–1542.
doi:10.2514/1.12401

[17] Aki, M., Waszak, M., and Shkarayev, S., "Development of Micro Air Vehicles with In-Flight Adaptive Wing," *Introduction to the Design of Fixed-Wing Micro Aerial Vehicles*, edited by T. J. Mueller, J. C. Kellogg, P. G. Ifju, and S. V. Shkarayev, AIAA, Reston, VA, 2006, pp. 241–275, Chap. 6.

[18] Kline, S. J., and McClintock, F. A., "Describing Uncertainties in Single-Sample Experiments," *Mechanical Engineering*, Vol. 75, No. 1, 1953, pp. 3–8.

[19] Barlow, J. B., Rae, W. H., Jr., and Pope, A., *Low-Speed Wind Tunnel Testing*, 3rd ed., Wiley, New York, 1999.